Journal of Power Sources 261 (2014) 120–135

Contents lists available at ScienceDirect

Journal of Power Sources

journal homepage: www.elsevier.com/locate/jpowsour

# Modeling of degradation effects considering side reactions for a pouch type Li-ion polymer battery with carbon anode

Rujian Fu [a], Song-Yul Choe [a,*], Victor Agubra [b], Jeffrey Fergus [b]

[a] 1418 Wiggins Hall, Mechanical Engineering, Auburn University, Auburn, AL, USA
[b] 273 Wilmore Laboratories, Materials Research and Education Center, Auburn University, Auburn, AL, USA

## HIGHLIGHTS

- We have experimentally characterized degraded cells by studying their capacities, impedances, morphologies and compositions.
- Based on the experimental findings, four degradation parameters are identified and a degradation model is developed.
- The deposits electronically isolate certain anode particles, reducing the amount of active anode and causing capacity fade.
- The resistance of the deposit layer estimated by the degradation model has the same trend as its thickness measured by SEM.

## ARTICLE INFO

*Article history:*
Received 9 October 2013
Received in revised form
3 January 2014
Accepted 13 March 2014
Available online 22 March 2014

*Keywords:*
Li ion polymer battery
Degradation model
Side reactions
SEI
Deposits
Capacity fade

## ABSTRACT

When a lithium ion polymer battery (LiPB) is being cycled, one major cause for degradations is the irreversible side reactions between ions and solvent of electrolyte taking place at the surface of anode particles. SEM analysis of cycled battery cells has revealed that the deposits from the side reactions are dispersed not only on particles, but also between the composite anode and the separator. Thus, the solid electrolyte interface (SEI) becomes thicker and extra deposit layers are formed between composite anode and separator. Also, XPS analysis showed that the deposits are composed of $Li_2CO_3$, which is ionic conductive and electronic nonconductive. Based on the mechanisms and findings, we identified four degradation parameters, including volume fraction of accessible active anode, SEI resistance, resistance of deposit layer and diffusion coefficient of electrolyte, to describe capacity and power fade caused by the side reactions. These degradation parameters have been incorporated into an electrochemical thermal model that has been previously developed. The terminal voltage and capacity of the integrated model are compared with experimental data obtained for up to 300 cycles. Finally, the resistance of the deposit layer calculated by the model is validated against the thickness of the deposit layer measured by SEM.
© 2014 Elsevier B.V. All rights reserved.

## 1. Introduction

The lithium ion battery has become the most preferred electrochemical energy storage device because of its high energy density, power density and columbic efficiency. When a cell is being cycled, there are various degradation processes that take place in different cell components as a function of operating conditions. These processes have not been well understood, so it is very hard to predict the life of the battery. One of the causes for degradation that has been identified is the side reactions caused by reduction of the electrolyte [1–8]. The side reactions take place in the region where the composite carbon anode is mixed with electrolyte and consumes lithium ions and the electrolyte solvents to produce deposits. The deposits cover anode particles, which reduces the active area and increase ionic resistance. As a result, capacity and power fade occur.

One of the causes for the side reactions at the anode is the low potential difference between electrode and electrolyte. When charging starts, the flow direction of ions is reversed from electrolyte to solid, so the potential between the electrode and electrolyte decreases [7]. When the potential across the anode and electrolyte is less than 0.5 V, a reduction process between the solvent of electrolyte and $Li^+$ is induced [8]:

$$S + 2Li^+ + 2e^- \rightarrow P$$

* Corresponding author. Tel.: +1 334 844 3328; fax: +1 334 844 3307.
*E-mail address:* choe@auburn.edu (S.-Y. Choe).

http://dx.doi.org/10.1016/j.jpowsour.2014.03.045
0378-7753/© 2014 Elsevier B.V. All rights reserved.

**Nomenclature**

| | |
|---|---|
| $A$ | sandwich area of the cell ($cm^2$) |
| $a_s$ | specific surface area of electrode ($cm^{-1}$) |
| $c_s$ | ion concentration in solid phase (mol $L^{-1}$) |
| $c_e$ | ion concentration in electrolyte (mol $L^{-1}$) |
| $C_p$ | heat capacity (J $kg^{-1}$ $K^{-1}$) |
| $D$ | diffusion coefficient ($cm^2$ $s^{-1}$) |
| $E_{chem}$ | electrochemical energy (J $cm^{-3}$) |
| $F$ | Faraday constant (96,487 C $mol^{-1}$) |
| $h_c$ | convective heat transfer coefficient (W $cm^{-2}$ $K^{-1}$) |
| $I$ | current of the cell (A) |
| $i$ | current density (A $cm^{-2}$) |
| $i_0$ | reference exchange current density (A $cm^{-2}$) |
| $j$ | reaction rate (A $cm^{-3}$) |
| $L$ | thickness of micro cell (cm) |
| $l$ | coordinate along the thickness of micro cell |
| $n$ | amount of Li ion (mol) |
| OCV | open circuit voltage (V) |
| $P_{chem}$ | power contributing to the increase of chemical energy (W $cm^{-3}$) |
| $Q_{max}$ | capacity of the cell (A h) |
| $q_{rev}$ | reversible heat generation rate (W $cm^{-3}$) |
| $q_{irr}$ | irreversible heat generation rate (W $cm^{-3}$) |
| $q_{convec}$ | heat convection rate (W $cm^{-3}$) |
| $R$ | resistance (Ω $cm^2$) or universal gas constant (8.3143 J $mol^{-1}$ $K^{-1}$) |
| $r_s$ | radius of spherical electrode particle (cm) |
| $r$ | coordinate along the radius of electrode particle (cm) |
| SOC | state of charge |
| $T$ | cell temperature (K) |
| $T_\infty$ | ambient temperature (K) |
| $t$ | time (s) |
| $U_{equi}$ | equilibrium potential (V) |
| $V$ | voltage (V) or volume of the composite electrode ($cm^3$) |
| $x$ | stoichiometric number in anode |
| $y$ | stoichiometric number in cathode |
| $t_+^0$ | initial transference number |

*Greek symbols*

| | |
|---|---|
| $\alpha$ | transfer coefficient for an electrode reaction |
| $\delta$ | thickness (cm) |
| $\varepsilon$ | volume fraction of a porous medium |
| $\phi_e$ | potential in electrolyte phase (V) |
| $\phi_s$ | potential in solid phase (V) |
| $\eta$ | surface overpotential of electrode reaction (V) |
| $\kappa$ | ionic conductivity of electrolyte (S $cm^{-1}$) |
| $\kappa_D$ | concentration driven diffusion conductivity (A $cm^{-1}$) |
| $\sigma$ | conductivity (S $cm^{-1}$) |

*Subscripts*

| | |
|---|---|
| cc | current collector |
| cell | micro cell |
| DL | deposit layer |
| EIS | measured by EIS |
| $e$ | electrolyte phase |
| max | maximum |
| $n$ | negative electrode (anode) |
| $p$ | positive electrode (cathode) |
| $r$ | radial direction in electrode particle |
| SEI | solid–electrolyte interface |
| SEM | measured by SEM |
| $s$ | solid phase |
| $T$ | terminal |
| 0% | 0% state of charge |
| 100% | 100% state of charge |

*Superscripts*

| | |
|---|---|
| eff | effective |
| Li | lithium ion |
| * | dimensionless |

where S denotes lithium ions and the solvent of electrolyte and P denotes the product that is deposited at the anode side [5–7]. In contrast, the potential at the cathode is high enough, so no electrolyte reduction can take place during either charge or discharge.

The deposits produced from the side reactions are composed of organic materials, such as $(CH_2OCO_2Li)_2$, and inorganic materials, such as $Li_2CO_3$ [7,8,10] and form a very thin extra film that adheres to the surface of the anode particles as solid electrolyte interface (SEI) [8]. Although the SEI is intentionally formed during the initial charging cycles by manufacturers, the side reactions continue and produce deposits that accumulate during cycling over a long time scale [1,4,9,10]. The accumulation of the deposits changes the thickness of the SEI. Since the deposits are ion conductive, the ionic resistance of the SEI increases, which leads to power fade. In contrast, these deposits are all electronic isolators [7,8,10] that completely isolate certain number of particles from electrons needed for chemical reactions so that these particles are no more available for active chemical reaction, which causes loss of active material and leads to capacity fade [3,4,7,21].

There have been various experimental attempts to characterize effects of side reactions on the morphology and compositions of materials using SEM, XRD, TEM, etc. [7–9,11–17]. In addition, electrochemical impedance spectroscopy (EIS) has been used to extract the electrochemical parameters [11,18,19].

On the other hand, there have been many approaches to theoretically analyze the degradation mechanism using electrochemical models, where changes of internal parameters subject to the degradation processes are considered [1–6,20,24,29].

Several authors have developed physical equations for the side reactions and incorporated them into electrochemical models [1,2,4]. Doyle et al. firstly proposed equations based on the Butler–Volmer equation that describe the side reactions that take place on the anode side [2], but no simulation was carried out. Based on the Dolye's work, Ramadass et al. developed a model for side reactions that is incorporated into electrochemical model and simulated capacity fade caused by loss of ions [1]. Both works described the side reactions based on the reaction current rate, $j^{Li}$, that is a sum of the intercalation and side reaction current. The amount of deposits from the side reactions is determined by integrating the side reaction current density. Sikha proposed a similar model for the side reactions, where effect of deposits on the porosity is considered [4]. However, none of the models aforementioned have considered the effects of deposits on capacity fade or have been validated experimentally.

Other authors have proposed semi-empirical models that are derived from experimental data collected at different stages of degradation, where the parameters are dependent upon operating conditions, particularly as functions of cycle number [3,5,6,21]. Typical parameters used for modeling the capacity fade are the anode SOC [3,4,21] and cathode SOC [3,4] that are adjusted at the

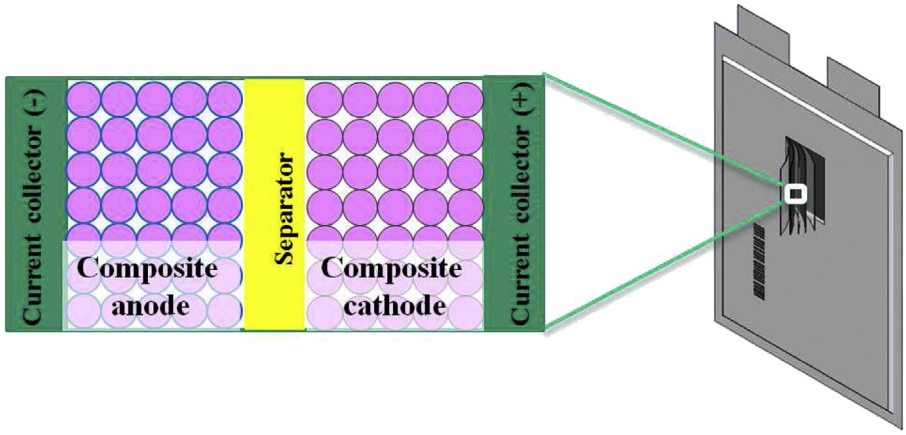


**Fig. 1.** Schematic diagram of the single cell (right) and micro cell (left) (the electrolyte is mixed with the composite electrodes and separator).

beginning of every cycle when the cell is fully charged. The diffusion coefficient of ion in electrode is used to model the decrease in rate capability [21] and the phenomena that the deposits clog pores in particles [4]. SEI resistance is used for modeling power fade [21]. Dependence of the parameters on temperature was investigated by Santhanagopalan et al. whereby the degradation process was accelerated in an elevated ambient temperature [3]. However, no solid physical evidence for selection and justification of the parameters are provided in the papers aforementioned.

In this work, the experimental analysis of the cycled cells conducted by SEM and XPS has shown that the side reactions produce deposits and are the major cause for performance fade. The deposits were placed not only on the surface of the SEI, but also formed thick layers at the interface between the composite anode and the separator. Based on these observations, we propose a degradation model that uses four key parameters: i) the volume fraction of accessible active anode, ii) SEI resistance, iii) resistance of deposit layer and iv) diffusion coefficient of electrolyte. The parameters are determined by experimental measurements. Particularly, the resistance of the deposit layer is estimated by measurement of the thickness of the deposit layer using SEM and compared with the calculated results from the model.

In addition to cycling, LiPBs also have calendar life which is a slow degradation process under open circuit conditions, but such degradation usually takes a long time (i.e. hundreds of days [5]), to affect the cell performance. In this work, large currents were used for cycling and each cycling test took less than two weeks. Therefore, the degradation process under open circuit is not considered in this work.

Beyond the side reactions involving electrolyte reduction and formation of deposits as described above, there are other causes for degradation that include crack formation and fracture of both electrodes due to stress generation at intercalation and de-intercalation processes of ions [15–17,23]. Fractured particles isolated from other part of the composite electrode may lose contact with current collector. The newly formed surface of the electrode left by the fractured particles continues participating in the side reactions [9,24,25–27]. In addition, there are several causes for degradation that include phase change of cathode active material with formation of oxide layer, lithium plating, decomposition of

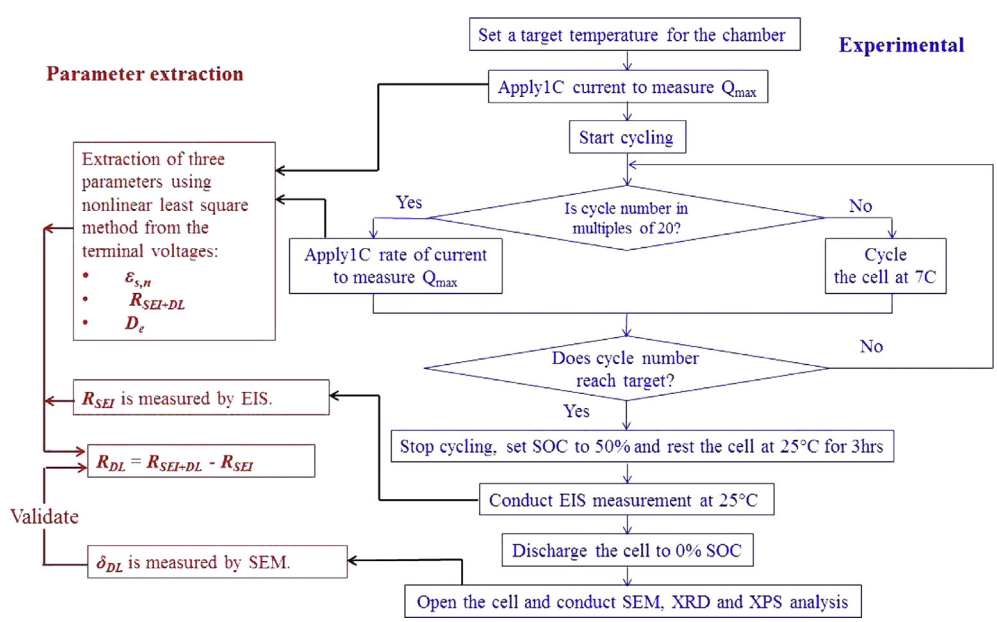


**Fig. 2.** Flow chart of experiment, parameter extraction and validation.

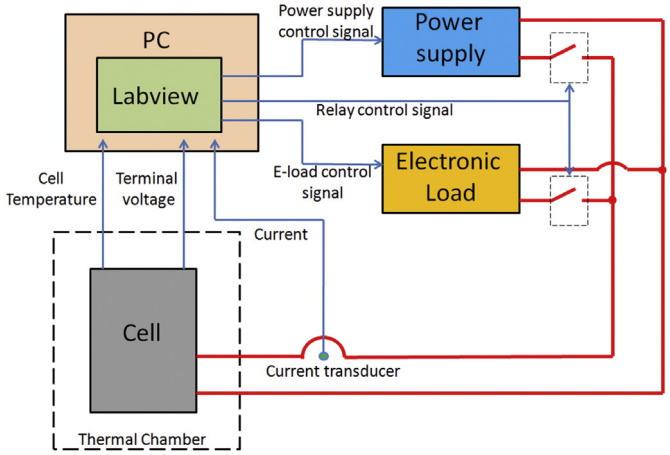


**Fig. 3.** Schematic diagram of a test station.

separator and others [22,28]. Since any significant role of these causes on degradation have not been observed in our experimental analysis, the effects are not considered in our study.

## 2. Experimental setup

The commercial LiPB cells studied in this work has a pouch type with dimensions of 164 mm × 250 mm × 5 mm. The single cell has 15.7 A h capacity and is composed of 30 micro cells connected in parallel, whose schematic diagrams are shown in Fig. 1. The active material of the anode and cathode are carbon and NMC (Li[MnNiCo]$O_2$), respectively. The polymer separator is made of PVdF. The electrolyte salt is $LiPF_6$ and its solvents are ethyl-methyl carbonates (EC) and dimethyl carbonate (DMC). Both electrode particles and the separator are mixed with the electrolyte.

The tests were conducted at three ambient temperatures: 40 °C, 25 °C and 0 °C. At each temperature, cells were charged and discharged with a 7C rate in order to accelerate degradation process and the number of cycles was 100, 200 and 300. In each cycle, the cell was discharged with a constant current until the terminal voltage decreased to 2.5 V and then charged with a constant current up to 4.15 V followed by a constant voltage (CV) charge until the magnitude of the current became 0.8 A. After every 20 cycles, a 1C discharge-resting-charge profile was applied to the cell to measure its capacity. The simulation results were fitted to the terminal voltage measured at this 1C cycle to estimate the degradation parameters. The ambient temperature was set as constant during the entire process as described above. The flow chart shown in Fig. 2 summarizes the procedures of testing, parameter estimation and validation.

A test station to conduct experiments was designed, constructed and calibrated. A schematic diagram of the test station is shown in Fig. 3, where a Sorensen DCS8-125E programmable power supply and a Kikusui PLZ1004W programmable E-load were used to generate charging and discharging profiles, respectively. They were connected in parallel to the battery cell and controlled by LabVIEW. Terminal current, voltage and temperature of the cell were measured and made available for estimation of capacity. Tests were conducted in a thermal chamber where the ambient temperature was controlled at 0 °C, 25 °C and 40 °C.

After cycling was finished, the cycled cells were sent to the EIS test station to measure their impedance spectra. Before starting EIS tests, the cells were set at 50% SOC by fully charging the cell and then discharging half of its capacity, where the capacity was measured with 1C current. A Gamry FC350 EIS system was used to measure the impedance spectrum. The system sends signals to a bipolar power supply to apply different frequencies of small AC excitation current and meanwhile senses the current flow as well as voltage of battery terminals to calculate the impedance at different frequencies. The AC current has amplitude of 1 A with frequency

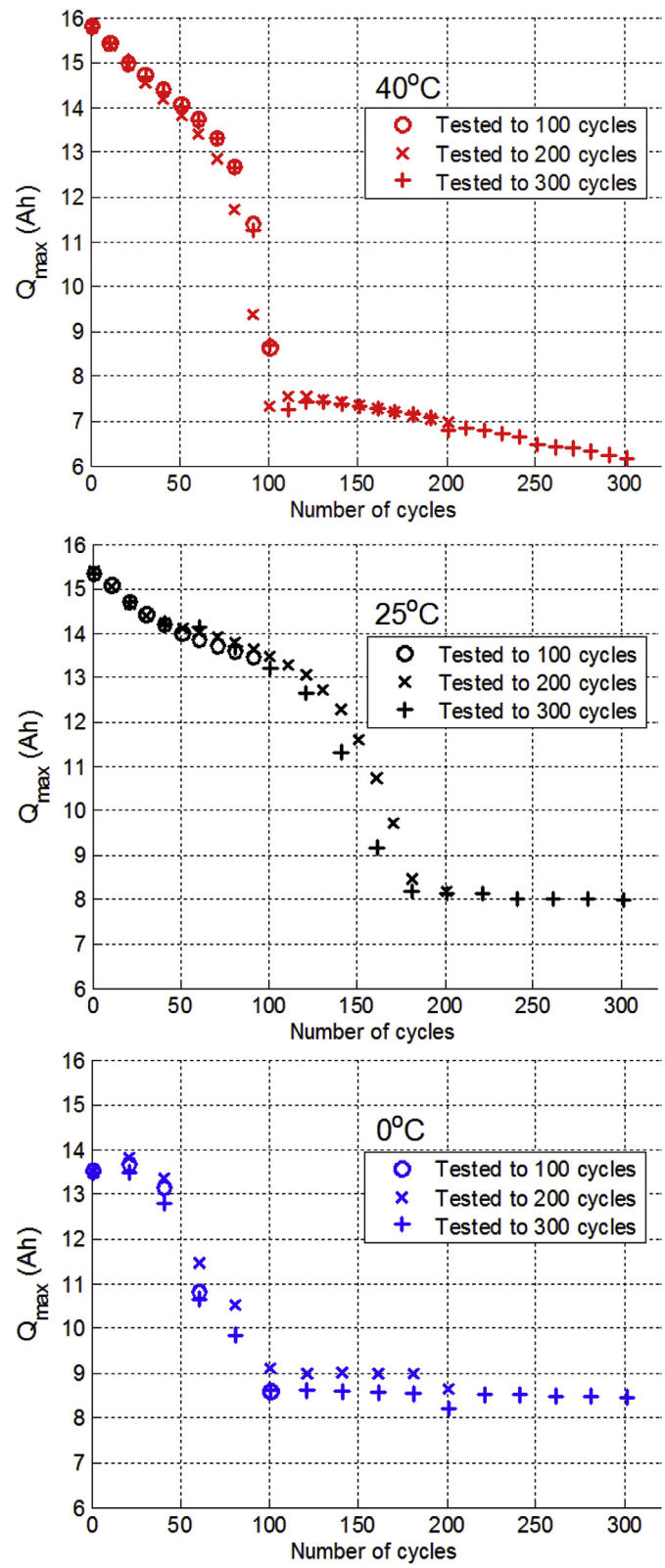


**Fig. 4.** Capacity vs. number of cycles at different temperatures.

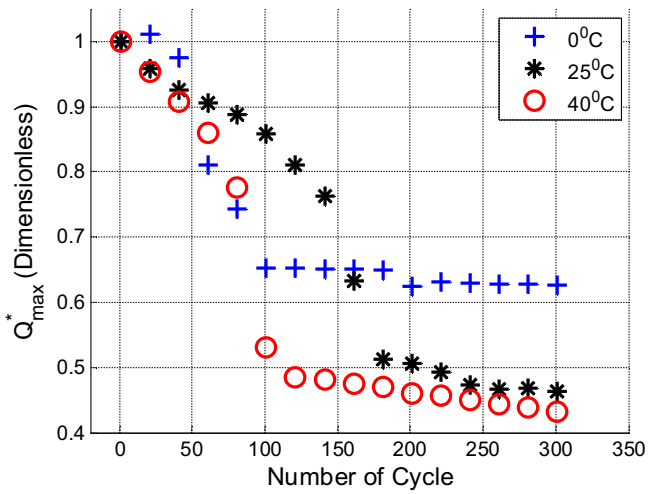


**Fig. 5.** Averaged dimensionless capacity vs. number of cycles at different temperatures.

region from 2 kHz to 1 mHz. The cell was enclosed in a chamber that maintains 25 °C ambient temperature during the EIS testing.

## 3. Experimental results and analysis

### 3.1. Analysis of capacity fade

The capacity of each cell, $Q_{max}$, is measured at 1C discharge current in every 20 cycles. The data are plotted in Fig. 4 as a function of number of cycles at 40 °C, 25 °C and 0 °C, where the degradation tests have good reproducibility at the same temperature. Generally, the capacity decreased when the number of cycles increased. At different temperatures, the initial capacity and the rate of capacity fade are different.

To better analyze capacity fades at different temperatures, a dimensionless capacity, $Q^*_{max}$, is introduced and defined as $Q_{max}$ of the degraded cell over $Q_{max}$ of the fresh cell

$$Q^*_{max} = \frac{(Q_{max})_{aged}}{(Q_{max})_{fresh}}. \quad (1)$$

After averaging $Q^*_{max}$ among the repeating tests, the averaged dimensionless capacity fades are plotted in Fig. 5 at different temperatures. The decreasing rate at the beginning was relatively high, especially for 40 °C and 0 °C, but became low when the cells have been cycled. The final capacity of cells at 300 cycles at 40 °C, 25 °C and 0 °C was 43.2%, 46.4% and 62.7%, respectively. This large fade of the capacity are most likely caused by charging the cells to a high SOC (100%) with a high current rate (7C) in every cycle.

### 3.2. Analysis of impedance spectrum and SEI resistance

The impedance characteristics of cycled cells measured by EIS at the different temperatures are plotted as markers in Fig. 6. The impedance of baseline plot measured from a fresh cell consists of a complete semicircle followed by a less obvious semicircle and a line with increasing slope. Compared to the baseline plot, the impedances of degraded cells are shifted to the right side with increased radius of the first semicircle. However, the effects of the number of cycles and temperature on impedance were not explicit. Therefore, an equivalent circuit model for EIS fitting (EIS-ECM) is used to extract a set of parameters that represent different electrochemical properties of the battery.

The EIS-ECM is similar to other model reported in the literature [30–33] and its configuration is shown in Fig. 7. In the model, $L$ is used to model the mutual inductance of external wires in high frequency domain (>1 kHz) [30,31]. $R_0$ is the ohmic resistance caused by electrolyte, deposit layer, separator, current collector and

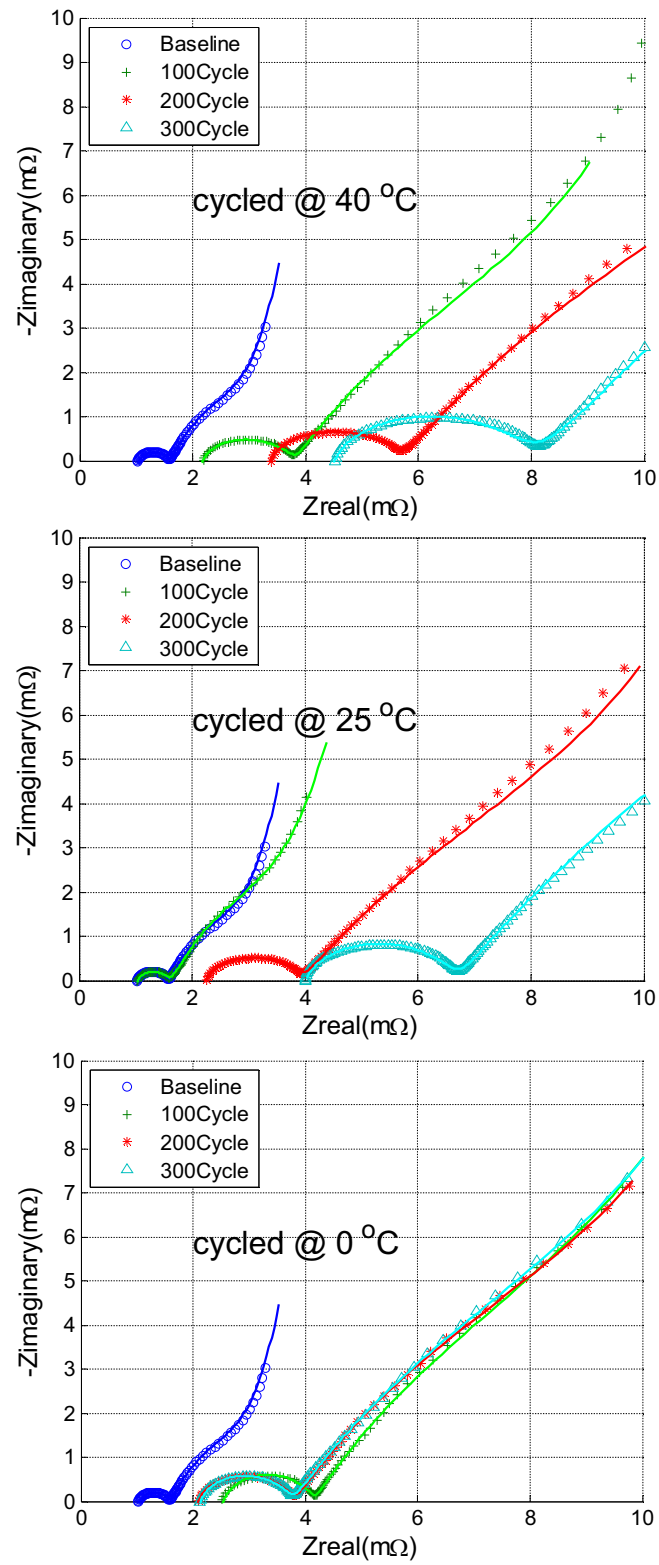


**Fig. 6.** Impedance characteristics measured by EIS (markers are measurement and lines are fitting by EIS-ECM).

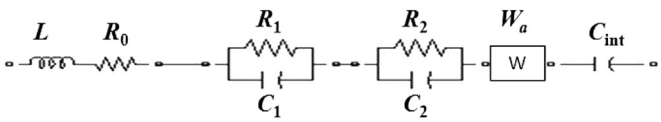


**Fig. 7.** EIS equivalent circuit model.

electrode, which equals to the left intercept between impedance spectrum and the *x*-axis at high frequency (≈1 kHz) [31–33]. $R_1$ and $C_1$ indicate SEI resistance and capacitance at anode, which dominate the shape of the first semi-circle in high frequency domain from 1 kHz to several Hz [30–33]. $R_2$ and $C_2$ indicate charge transfer resistance and double layer capacitance, respectively. They affect the shape of the second semi-circle, which is less obvious in the lower frequency range (several Hz to several mHz) [31,32]. $W_a$ is the Warburg admittance that represents ion diffusion in the electrolyte [30–32] and $C_{int}$ is the intercalation capacitance that indicates the process of ion intercalation [31,32]. Both $W_a$ and $C_{int}$ dominate the impedance spectrum in the low frequency region (<several mHz). To extract these parameters, the EIS-ECM is fitted to the impedance spectrum measured by EIS using simplex algorithm. The simulated impedance spectra are then plotted as lines in Fig. 6 in comparison with the experimental data.

In this work, the EIS parameter that is most relevant to the degradation model is the SEI resistance. It is extracted and plotted as a function of cycles and temperature, as shown in Fig. 8. The dots and bars indicate the mean value and standard deviation,

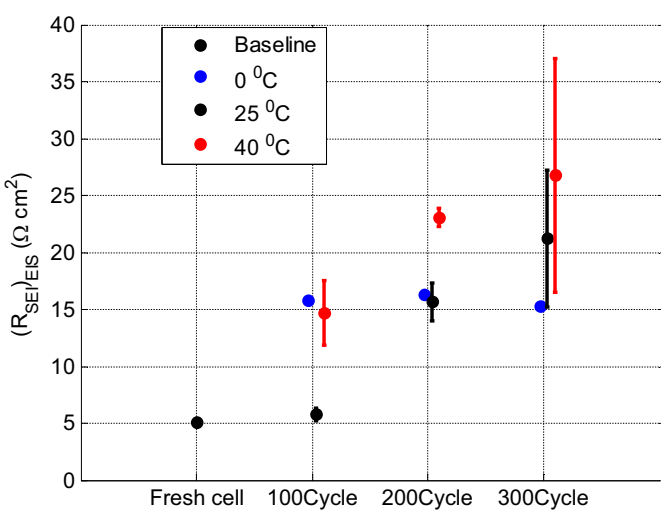


**Fig. 8.** SEI resistance estimated by EIS.

respectively, of $(R_{SEI})_{EIS}$ of cells from the repeating tests. The increase of the resistance was dependent upon the number of cycles and temperature. At 40 °C and 25 °C, $(R_{SEI})_{EIS}$ increased with increasing number of cycles and ambient temperatures. The resistance increased up to four times larger than that of the fresh cell. At 0 °C, the data shows that most degradation took place between 0 and 100 cycles and the changes of $(R_{SEI})_{EIS}$ among 100, 200 and 300 cycled cells are relatively small.

### 3.3. Analysis of morphology and composition

To investigate any changes of material compositions and morphologies of the cycled cells, the cycled cells were then discharged and opened. The separators in degraded cells were found dry, which is most likely caused by consumption of electrolyte due to the side reactions. For each single cell, multiple small samples were cut from different locations in the globe box with a high purity argon atmosphere. The separators were removed from anode and cathode samples when conducting morphology and composition analysis. Two images for anode side of the fresh and degraded cell taken by SEM are shown in Fig. 9. The anode particles of the cycled cells were coated by white deposits. These deposits are dispersed randomly all over the carbon surface in a non-uniform manner and its coverage ratio does not change significantly from cell to cell.

SEM was then used to take images for cross sections of the anode, as shown in Fig. 10, where the middle and the right images are the cross-sections of a fresh anode and a degraded anode, respectively. Section A is the composite anode with negative current collector embedded inside. The separators are located at section B, but were removed when the images were taken. Section C indicates layers of the deposit that is called "Deposit Layer".

The SEM images of the cycled cells are used to measure the thickness of the deposit layers, $\delta_{DL}$, that are depicted as a function of the number of cycles and temperature, as shown in Fig. 11. The thickness of the deposit layers is in tens of micrometers compared to that of the SEI which is typically several nanometers.

The composition of the deposit layers was evaluated using XPS, a spectrum from which is shown in Fig. 12, where the peaks of Li1s, C1s and O1s are identified. Zoomed-in spectra are shown in Fig. 13, where the binding energies for Li1s, C1s and O1s are shown. These binding energies are then summarized in Table 1, including those characterized in $Li_2CO_3$ by Contarni [34] and Contour [35]. Comparison in the table shows that the binding energies measured for Li1s, C1s and O1s correspond to those found in the two standard $Li_2CO_3$ studies [34,35] indicating the deposit layer should have a composition of $Li_2CO_3$, which is also a major composition of SEI [7,8,10]. The deposits of the side reactions not just form SEI, but also form thick deposit layers between composite anode and separator.

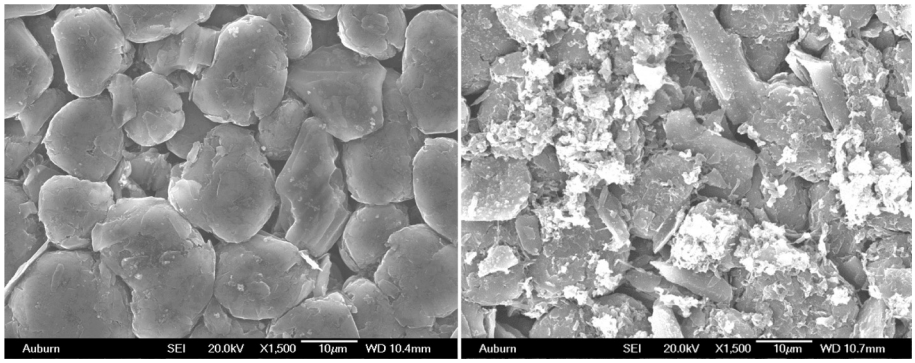


**Fig. 9.** SEM image of a fresh anode (left) and a degraded anode after 300 cycles at 25 °C (right).

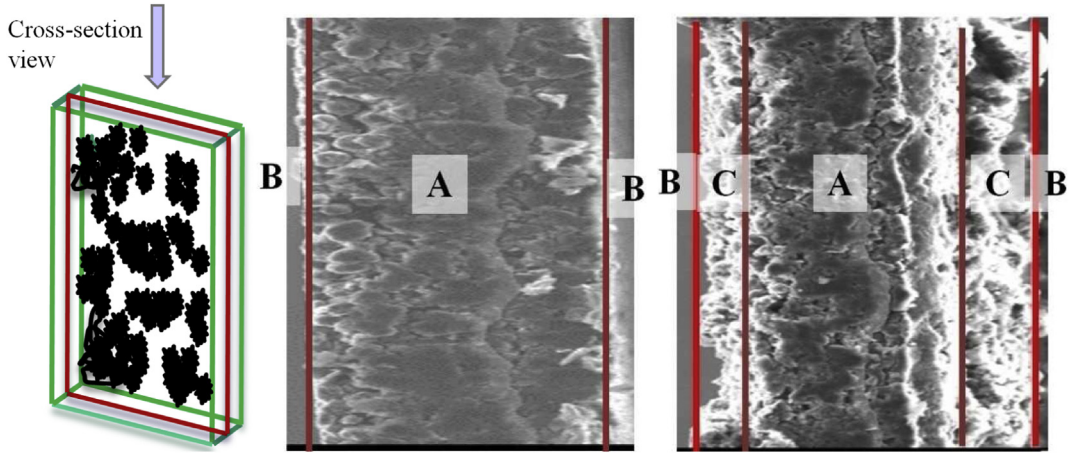


**Fig. 10.** SEM of cross-section of a fresh anode (middle) and a degraded anode after 300 cycles at 25 °C (right).

SEM images of fresh and degraded cathode are shown in Fig. 14 and reveal no significant changes. The XRD spectra in Fig. 15 also show no phase change or new phase formation in the active materials of anode and cathode.

The results observed from analysis of the cycled cells are summarized as below:

i. Large amount of deposits are formed at the surface of anode particles.
ii. The deposits also forms thick deposit layers between the composite anode and the separator.
iii. The deposits contain $Li_2CO_3$.
iv. The separator dries out.
v. No phase change in active material of anode and cathode is observed.
vi. SEI resistance is increased according to the EIS measurement.

Based on the experimental results, the following statements have been drawn:

a) Since $Li_2CO_3$ films act as electronic isolators [7,8,10], based on i and iii and other investigations [3,4,6,7,21], the deposits can completely isolate certain anode particles from electrons, so that these particles are no more available for active chemical reactions, which causes loss of active material and leads to capacity loss.
b) Based on v, the degradation of active materials is negligible and no effect on capacity fade can be assumed.
c) Based on i and vi as well as other investigations [1,4,8–10], the deposits accumulate on the anode particles, which leads to growth of SEI layers and consequently an increase in internal resistance.

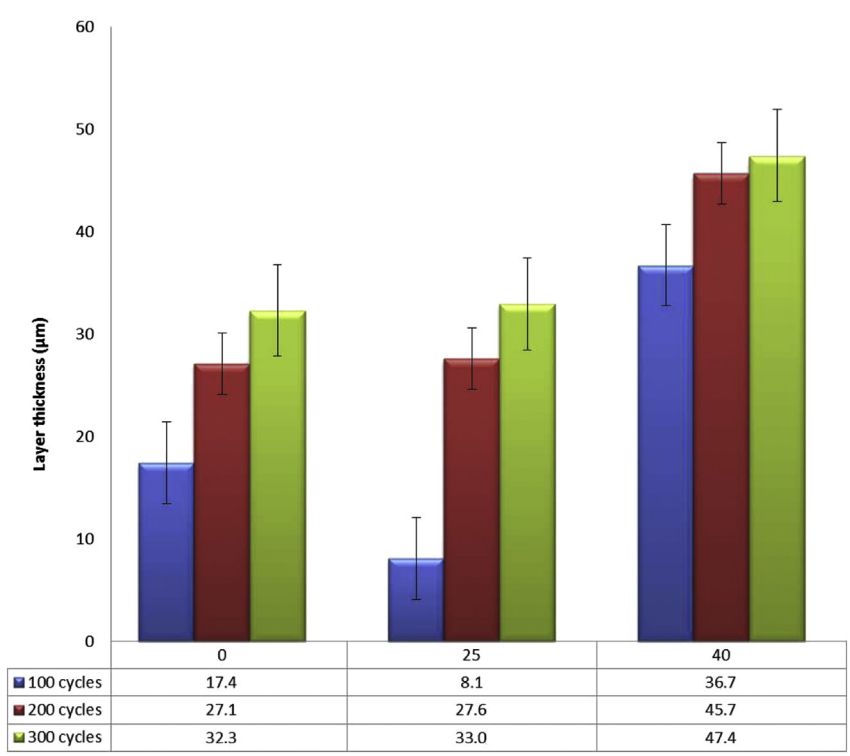


**Fig. 11.** Thickness of the deposit layers.

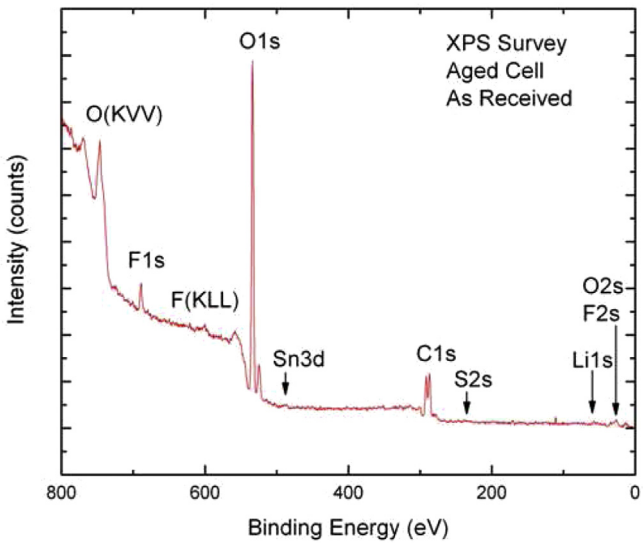


**Fig. 12.** XPS spectra derived from the deposit layer.

d) Based on ii and iii, the deposit layer has much lower ion conductivity than that of electrolyte and extra internal resistance is induced by the deposit layer.
e) Based on iv, the electrolyte is being consumed, which may lead to decrease in diffusion coefficient of electrolyte and extra internal resistance.

In summary, the anode, rather than cathode, is adversely affected by the deposits produced by the side reactions. No significant changes were observed regarding active anode and cathode material. Therefore, we have concluded that the side reactions at anode side and its deposit are the major causes for capacity loss in Fig. 5 and increase in internal resistance in Fig. 8. The proposed degradation model is developed based on the experimental results as aforementioned and explained in the next section.

## 4. Setup for modeling

### 4.1. Development of the electrochemical thermal model

The cell is mathematically described by a one dimensional sandwiched model, which was developed in previous work [23,36]. The model is composed of a composite anode mixed with electrolyte, a separator and a composite cathode mixed with electrolyte. The electrode materials are porous. When the cell is charged or discharged, electrons go through external circuit while ions are transported in the electrode and electrolyte. Chemical reactions take place at the surface of electrode particles that contact the electrolyte, followed by ion diffusion inside the electrode particles. The model has three temperature-dependent parameters including exchange current density, SEI resistance and diffusion coefficient of electrode particle, whose temperature dependency are obtained empirically. In addition, three heat source terms are considered for temperature behavior that include change of entropy, Joule heating and heat of mixing. The equations and boundary conditions are summarized in Table 2.

**Table 1**
Binding energies (eV) for lithium carbonate, $Li_2CO_3$.

| Investigator | C1s | Li1s | O1s |
|---|---|---|---|
| This work | 289.5 | 55.0 | 531.3 |
| Contarni [34] | 289.55 | 55.12 | 531.40 |
| Contour [35] | 289.80 | 55.20 | 531.50 |

### 4.2. Development of the semi-empirical degradation model

Schematic diagrams for a fresh cell and degraded cell are depicted in Fig. 16, where the circles with blue color (in the web version) on the anode particles represent the SEI layer. In the degraded cell, thicker blue circles indicate the growth of SEI layer due to the formation of deposits. The particles that are completely isolated by the deposits are marked by extra red (in the web version) crosses to indicate particles inaccessible to electrons needed for chemical reactions. The thick bar on the left of the separator indicates the deposit layer.

The changes of properties of the cell are considered in four degradation parameters: the volume fraction of accessible active anode, SEI resistance, resistance of deposit layer and diffusion coefficient of electrolyte. In addition, after the cell is degraded, the overall thickness of the micro cell is increased due to the formation of the deposit layer, while the thickness of composite anode, separator and composite cathode are regarded as constant.

Since the deposits of side reactions are electronic isolators, some anode particles can be completely isolated by the deposits and become inaccessible for electrons anymore and therefore, the amount of accessible anode decreases. This phenomena causes capacity fade and is approximated by decreasing the volume fraction of accessible active material, $\varepsilon_{s,n}$. $\varepsilon_{s,n}$ affects the specific area of the anode

$$a_{s,n} = \frac{4\pi r_s^2}{4/3\pi r_s^3}\varepsilon_{s,n} = 3\frac{\varepsilon_{s,n}}{r_s} \tag{2}$$

where $a_{s,n}$ equals to the ratio of particle area to particle volume multiplied by $\varepsilon_{s,n}$ and $r_s$ is the radius of electrode particles. In

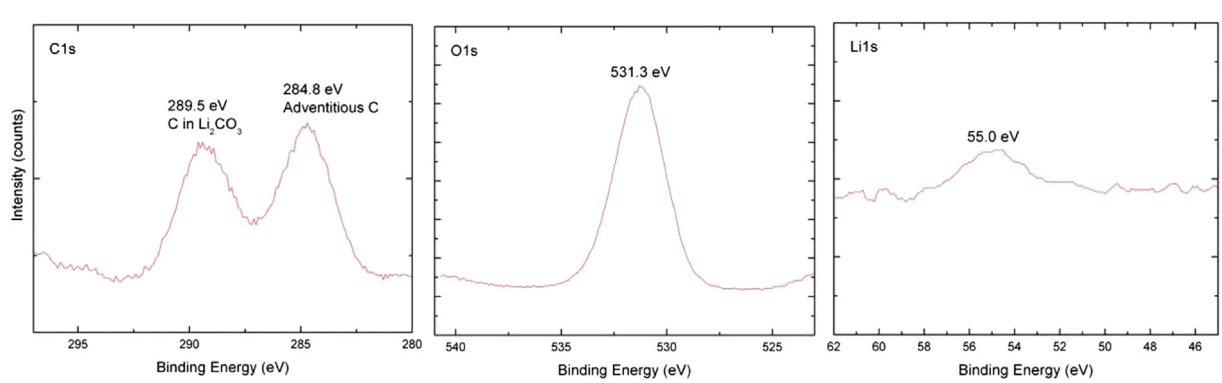


**Fig. 13.** Zoomed in XPS spectra derived from the deposit layer.

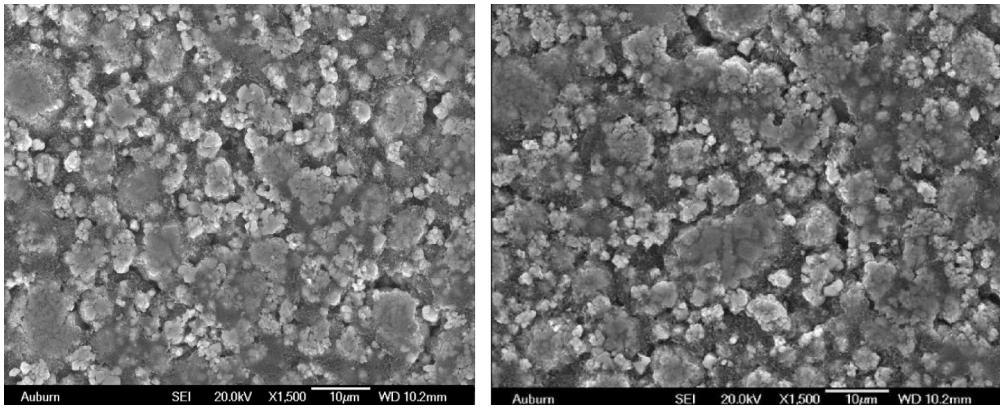


**Fig. 14.** SEM images of a fresh cathode (left) and a degraded cathode after 300 cycles at 25 °C (right).

addition to $\varepsilon_{s,n}$, no other degradation parameters are used to model capacity fade.

The deposits are conductive to ions so the growth of the SEI results in an increase of internal resistance and leads to power fade. Increased SEI resistance, $R_{SEI}$, is reflected in change of the activation overpotential, $\eta_{s,n}$

$$\eta_{s,n} = \phi_{s,n} - \phi_{e,n} - U_{equi,n} - \frac{R_{SEI}}{a_{s,n}} j^{Li} \tag{3}$$

where $\phi_{s,n}$ and $\phi_{e,n}$ are the anode and electrolyte potential, $U_{equi,n}$ is the equilibrium potential of anode and $j^{Li}$ is the reaction rate.

The deposit layer formed between the separator and the composite anode which has a similar chemical composition as that of SEI. Even though the layers are ion conductive, overall ionic resistance of this extra layer is larger than that of pure electrolyte. Consequently, the total internal resistance increases and power fade occurs. The extra voltage drop caused by the resistance of the deposit layer is calculated using the ionic current that passes through the composite anode and is expressed with $\int_0^{\delta_n} j^{Li}(l)\mathrm{d}l$. The terminal voltage is as follows

$$V_T = \phi_s|_{l=L} - \phi_s|_{l=0} - R_{cc} i - R_{DL} \int_0^{\delta_n} j^{Li}(l)\mathrm{d}l \tag{4}$$

where $V_T$ is the terminal voltage, $R_{cc}$ is the resistance of current collector, $\delta_n$ is the thickness of composite anode and $i$ denotes the current density of the micro cell that represents electron current. The current density in the last term has the same magnitude as that of the electron current.

Both $R_{SEI}$ and $R_{DL}$ contribute to the internal resistance for the battery and it is impossible to separately measure the individual value based on the terminal data acquired from cycling. For parameter estimation of the model, $R_{SEI}$ and $R_{DL}$ are regarded as one value. $R_{SEI}$ in Eq. (3) has a unit of $\Omega\ \mathrm{cm}^2$, where $\mathrm{cm}^2$ denotes the total area at the anode side where chemical reactions are taking place. $R_{DL}$ in Eq. (4) has a unit of $\Omega\ \mathrm{cm}^2$, but $\mathrm{cm}^2$ denotes the sandwich area of the cell. Therefore, the differences in the unit of $R_{SEI}$ and $R_{DL}$ need to be adjusted by reformatting the equations. First define $dV_{SEI}$ as the voltage drop on SEI in a differential volume of composite anode

$$\mathrm{d}V_{SEI} = \frac{j^{Li}(l)}{a_{s,n}} \frac{R_{SEI}\mathrm{d}l}{\delta_n} \tag{5}$$

where $l$ is the coordinate to the thickness direction of composite anode. Then the total voltage drop on SEI, $V_{SEI}$, is obtained by integrating $dV_{SEI}$ over the thickness of composite anode

$$V_{SEI} = \int \mathrm{d}V_{SEI} = \int_0^{\delta_n} \frac{j^{Li}(l)}{a_{s,n}} \frac{R_{SEI}\mathrm{d}l}{\delta_n}. \tag{6}$$

Under assumption that the specific area of the anode and the thickness of SEI is independent upon the $l$ coordinate of the anode, the voltage drop becomes

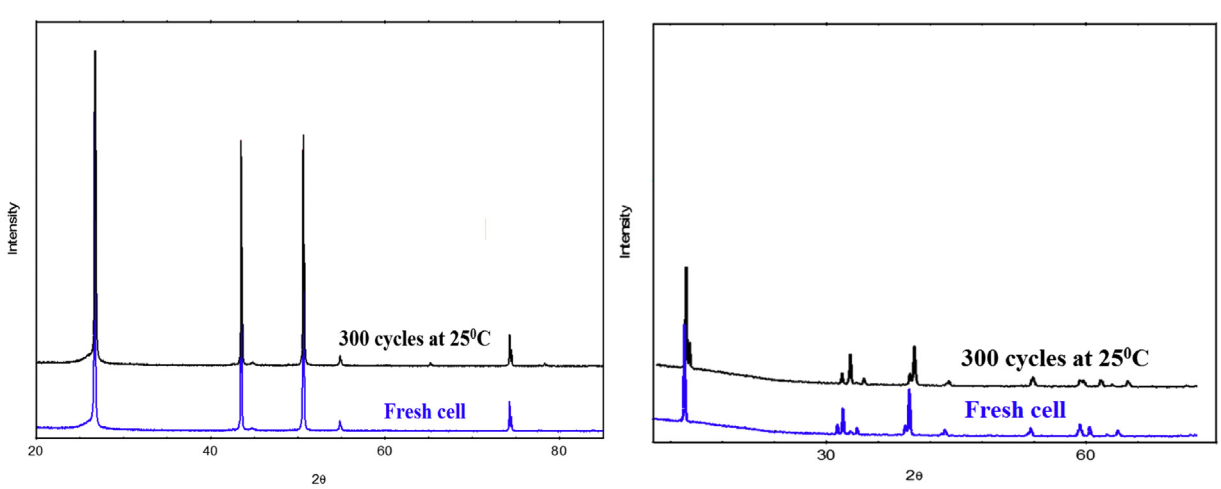


**Fig. 15.** XRD analysis of anode active material (left) and cathode active material (right).

**Table 2**
The electrochemical-thermal model.

| Conservation equations | Boundary conditions |
|---|---|
| Ion conservation in electrode<br>$\frac{\partial c_s}{\partial t} = D_s\left(\frac{\partial^2 c_s}{\partial r^2} + \frac{2}{r}\frac{\partial c_s}{\partial r}\right)$ | $r^2\frac{\partial c_s}{\partial r}\Big\vert_{r=0} = 0 \quad -D_s\frac{\partial c_s}{\partial r}\Big\vert_{r=r_s} = \frac{j^{Li}}{a_s F}$ |
| Ion conservation in electrolyte<br>$\frac{\partial(\varepsilon_e c_e)}{\partial t} = \frac{\partial}{\partial l}\left(D_e^{eff}\cdot\frac{\partial}{\partial l}c_e\right) + \frac{1-t_p^0}{F}j^{Li} = 0$ | $\frac{\partial c_e}{\partial l}\Big\vert_{l=0} = \frac{\partial c_e}{\partial l}\Big\vert_{l=L} = 0$ |
| Charge conservation in electrode<br>$\frac{\partial}{\partial l}\left(\sigma_s^{eff}\cdot\frac{\partial}{\partial l}\phi_s\right) = j^{Li}$ | $-\sigma_{s,n}^{eff}\frac{\partial\phi_s}{\partial l}\Big\vert_{l=0} = -\sigma_{s,p}^{eff}\frac{\partial\phi_s}{\partial l}\Big\vert_{l=L} = \frac{I}{A}$<br>$\frac{\partial\phi_s}{\partial l}\Big\vert_{l=\delta_n} = \frac{\partial\phi_s}{\partial l}\Big\vert_{l=\delta_p} = 0$ |
| Charge conservation in electrolyte<br>$\frac{\partial}{\partial l}\left(\kappa_e^{eff}\cdot\frac{\partial}{\partial l}\phi_e\right) + \frac{\partial}{\partial l}\left(\kappa_D^{eff}\cdot\frac{\partial}{\partial l}(\ln c_e)\right) + j^{Li} = 0$ | $\frac{\partial\phi_e}{\partial l}\Big\vert_{l=0} = \frac{\partial\phi_e}{\partial l}\Big\vert_{l=L} = 0$ |
| *Electrochemical kinetics* | |
| Equilibrium potentials | |
| $U_{equi,n}(x) = 8.00229 + 5.0647\,x - 12.578\,x^{1/2} - 8.6322\,e - 4x^{-1} + 2.1765\,e - 5x^{3/2} - 0.46016\ \exp(15(0.06-x)) - 0.55364\ \exp(-2.4326(x-0.92))$ | |
| $U_{equi,p}(y) = U_{OCV\ (experiment)} + U_{equi,n}(x)$ | |
| Butler–Volmer equation<br>$j^{Li} = a_s i_0\frac{(\alpha_a+\alpha_c)F}{RT}\eta$ | Activation overpotential<br>$\eta = \phi_s - \phi_e - U_{equi}$ |
| *Energy and heat equations* | |
| Energy equation (lumped model)<br>$C_p m\frac{\partial T}{\partial t} = \int_V q_{rev}dV + \int_V q_{irr}dV + \int_A q_{convec}dA$ | Reversible heat generation rate<br>$q_{rev} = j^{Li}\cdot T\cdot\frac{\partial U_{OCV}}{\partial T}$ |
| Irreversible heat generation rate<br>$E_{chem} = -\frac{3\varepsilon_{s,p}FN\delta_p\int_0^{r_s}c_{s,p}\cdot U_{equi,p}r^2dr}{\delta_{cell}r_s^3} - \frac{3\varepsilon_{s,n}FN\delta_n\int_0^{r_s}c_{s,n}\cdot U_{equi,n}r^2dr}{\delta_{cell}r_s^3}$<br>$p_{chem} = \frac{dE_{chem}}{dt} \quad q_{irr} = -\frac{V_T i}{\delta_{cell}} - P_{chem}$<br>Heat convection rate $q_{convec} = h_c(T - T_\infty)$ | |

$$V_{SEI} = \frac{R_{SEI}}{a_{s,n}\delta_n}\int_0^{\delta_n} j^{Li}(l)dl. \tag{7}$$

Since the magnitude of the ionic current, $\int_0^{\delta_n} j^{Li}(l)dl$, is equal to that of the current density of cell $i$, the equivalent SEI resistance, $R'_{SEI}$, is obtained based on Eq. (7), where the resistance has a unit of $\Omega\ cm^2$ and $cm^2$ denotes the sandwich area

$$R'_{SEI} = \frac{R_{SEI}}{a_{s,n}\delta_n}. \tag{8}$$

Then $R_{SEI}$ and $R_{DL}$ can be regarded as series connected and a resistance

$$R_{SEI+DL} = R'_{SEI} + R_{DL} = \frac{R_{SEI}}{a_{s,n}\delta_n} + R_{DL}. \tag{9}$$

Since the side reactions consume the solvent of electrolyte and Li ions, the separator of cycled cells becomes dry. The dryness of the separator is considered by decreasing diffusion coefficient of electrolyte, $D_e$ and consequently the effective diffusion coefficient of electrolyte, $D_e^{eff}$.

$$D_e^{eff} = D_e\cdot\varepsilon_e \tag{10}$$

where $\varepsilon_e$ is the porosity (i.e., volume fraction of electrolyte).

In addition, the side reactions continuously consume lithium ions. When a battery is charged, the stoichiometric number for cathode, $y$, decreases to $y_{min}$, and the number for anode, $x$, becomes less than $x_{max}$ because of the loss of ions. Therefore, OCV becomes smaller than ideal maximum value of OCV and the battery is continuously charged until OCV reaches the ideal OCV. Likewise, when a battery is discharged, $x$ decreases to $x_{min}$ and $y$ becomes less than $y_{max}$ because of the loss of ions. Therefore, OCV becomes larger than the ideal minimum value of OCV and the battery is continuously discharged until OCV reaches the ideal OCV. These extra charging and discharging processes as described should have affected the calculation of the actual capacity of the degraded battery. However, detailed analysis and experimental validation will be needed to verify this calculation.

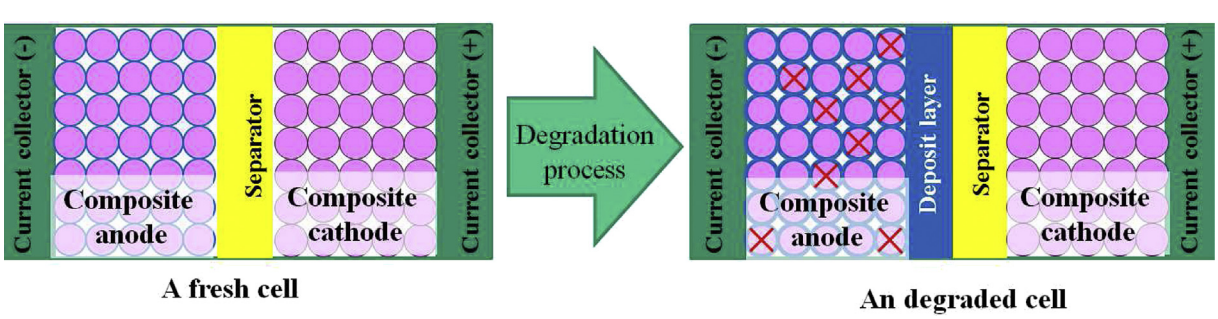


**Fig. 16.** The degradation processes involved in the anode side reactions.

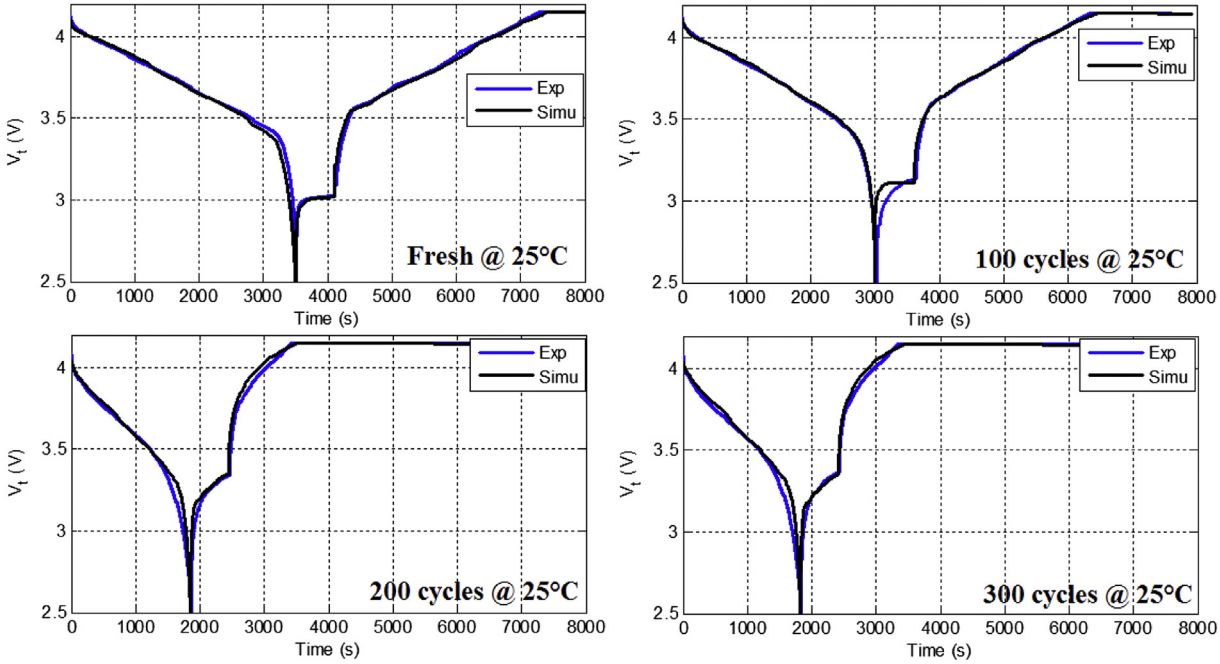


**Fig. 17.** Comparison of the terminal voltage at 1C discharge-rest-charge cycle at 25 °C.

## 5. Simulation, analysis and validation

### 5.1. Optimal estimation of three parameters for degradation model

Extra 1C discharge-resting-charge cycles were applied in every 20 cycles during cycling, where the terminal voltage was measured to find those parameters, as shown in Fig. 2. The parameters are estimated by employing the nonlinear least square method that minimizes the error of the terminal voltage between the degradation model and the experiment. The solver for the method was trust-region-reflective algorithm. The resulting three parameters are estimated every 20 cycles, so that 15 sets of parameters are available up to 300 cycles at each temperature. Comparison of the terminal voltage at 0, 100, 200 and 300 cycles is shown in Fig. 17, where 1C discharge-rest-charge cycle was applied and the ambient temperature was 25 °C. As the number of cycles increases, the duration needed for discharging decreases due to the loss of the active materials and as a result the capacity fade occurs. In addition, the magnitude of the voltage increases during charging and decreases during discharging, which are caused by increased resistance of SEI and the deposit layer as well as decreased diffusion coefficient. Consequently, power fade takes place.

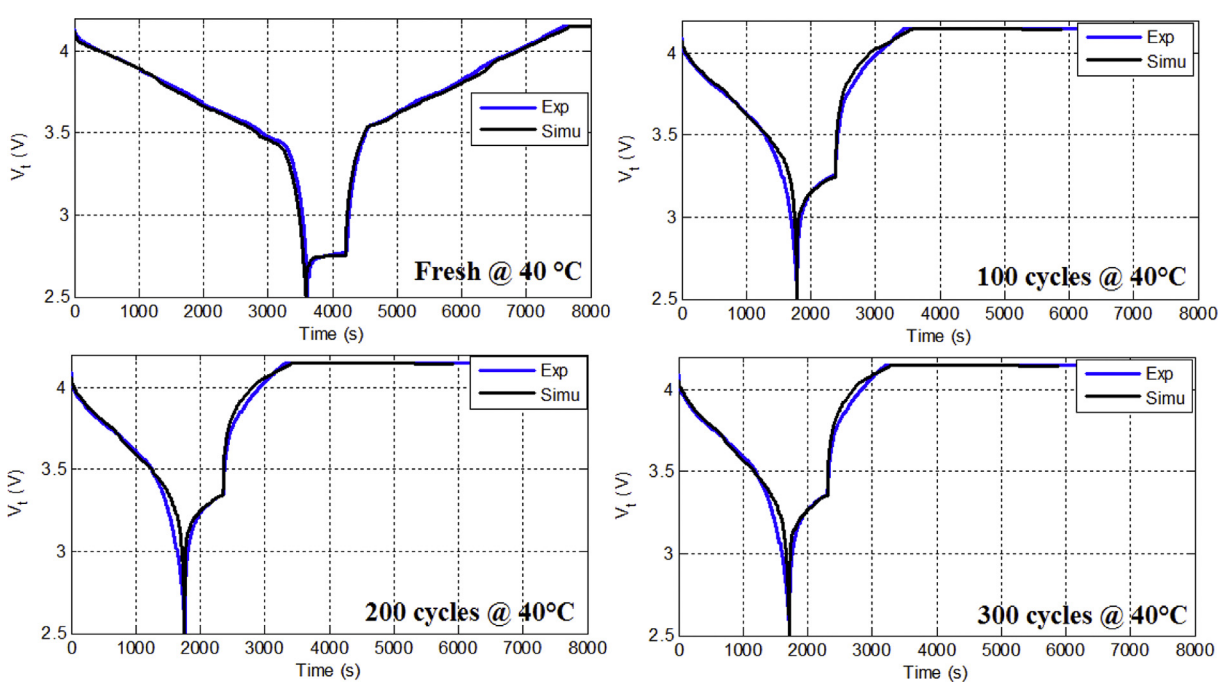


**Fig. 18.** Comparison of the terminal voltage at 1C discharge-rest-charge cycle at 40 °C.

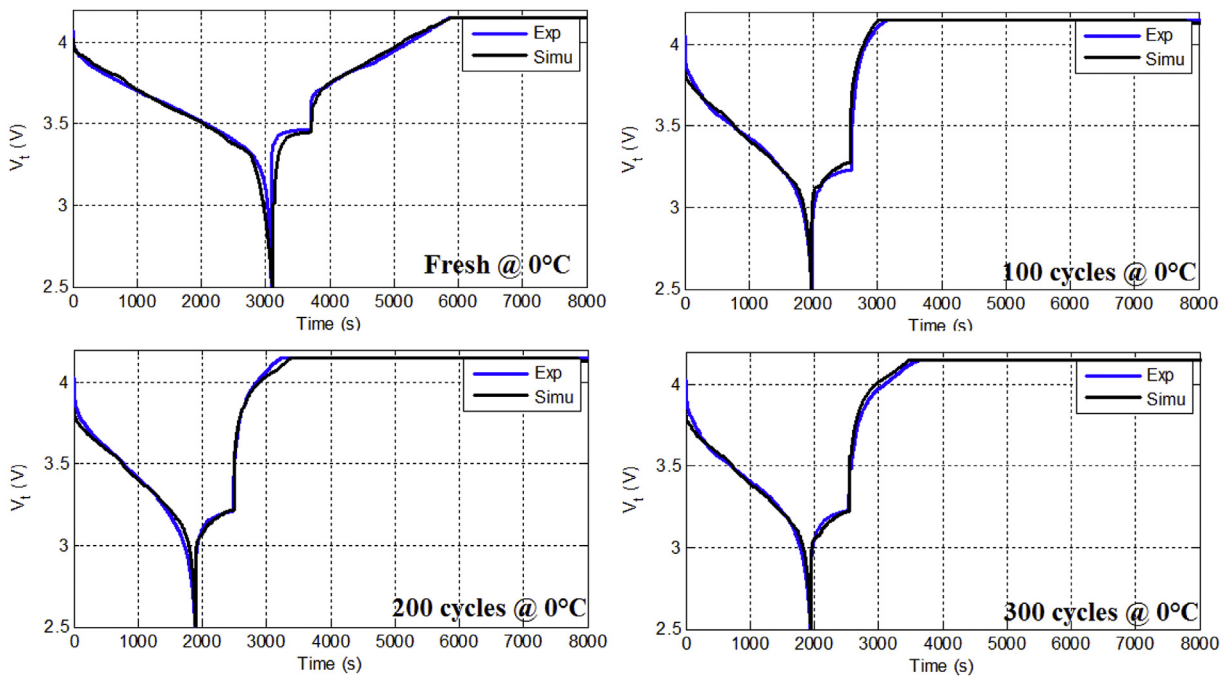


**Fig. 19.** Comparison of the terminal voltage at 1C discharge-rest-charge cycle at 0 °C.

The three parameters for the ambient temperature at 40 °C and 0 °C are estimated. Comparisons of the terminal voltage for the two temperatures at the different cycles are shown in Figs. 18 and 19. The trend of the terminal voltage is similar to that at 25 °C, but the degradation process became faster than that at 40 °C. At 0 °C, the terminal voltage during discharge becomes smaller and the CV charge takes much longer because the internal resistance increases at lower temperature. However, it does not mean necessarily that the degradation process became more severe at 0 °C.

### 5.2. Analysis of effects of the parameters on performance

The three parameters estimated above from the terminal voltage during cycling are the volume fraction of the active materials, the consolidated resistance for SEI and deposit layer, and the diffusion coefficient of electrolyte. The error bars shown in plots indicate 95% of the confidence intervals of parameters, which is calculated using the degradation model.

The dimensionless volume fraction of the active material, $\varepsilon^*_{s,n}$, is defined as $\varepsilon_{s,n}$ of the degraded cell over $\varepsilon_{s,n}$ of the fresh cell as a function of the number of cycles and ambient temperatures, which is plotted in Fig. 20. $\varepsilon^*_{s,n}$ decreases as the number of cycles increases, but depends upon the temperature. The decrease in $\varepsilon^*_{s,n}$ can be caused by deposits that isolate some particles from the anode electrode. At 25 °C, $\varepsilon^*_{s,n}$ has mostly decreased during the first 200 cycles, but at 40 °C and 0 °C, most loss in $\varepsilon^*_{s,n}$ happens during the first 100 cycles. In addition, elevated temperature induces a higher loss of active materials eventually.

Comparison between $\varepsilon_{s,n}$ in Fig. 20 and capacity fade in Fig. 5 shows a similar decreasing trend, so $\varepsilon_{s,n}$ plays the important role

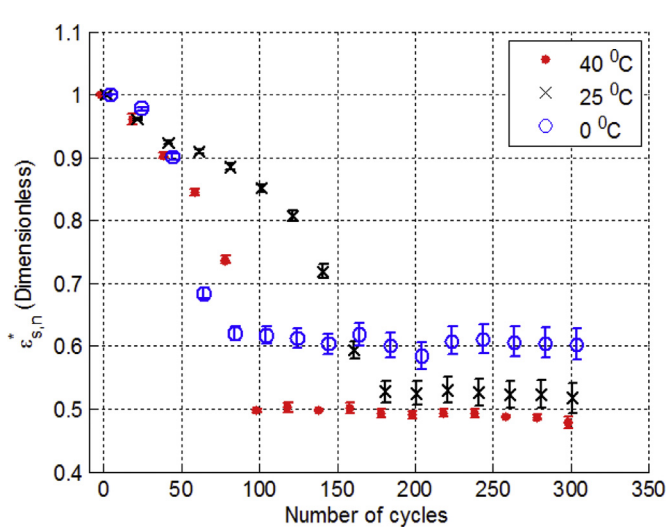


**Fig. 20.** Volume fraction of accessible anode vs. number of cycles at different temperatures.

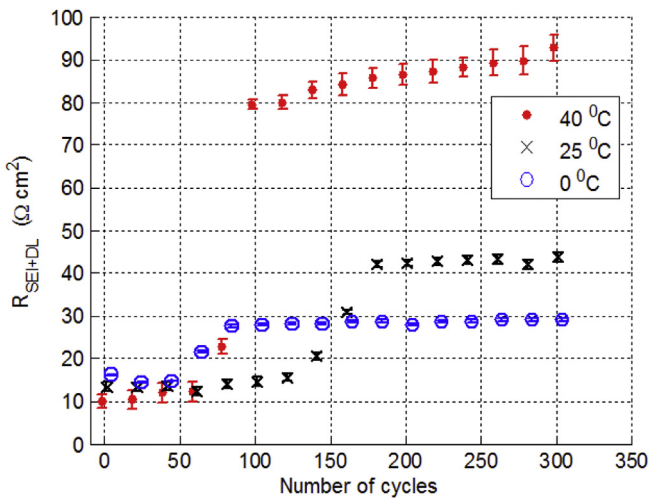


**Fig. 21.** Resistance of SEI and deposit layer vs. number of cycles at different temperatures.

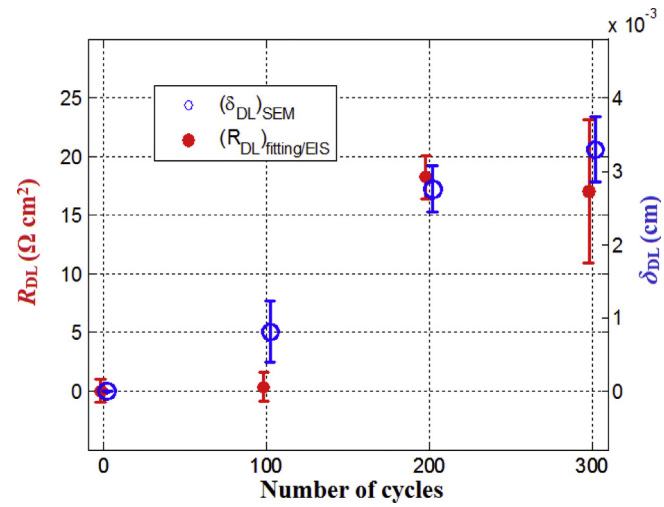


**Fig. 23.** $R_{DL}$ vs. $(\delta_{DL})_{SEM}$ for cells cycled at 25 °C.

for the capacity fade. When a cell is discharged by a constant current $I$ for a duration $\Delta t$, the final Open Circuit Voltage (OCV) can be calculated by

$$\mathrm{OCV} = U_{\mathrm{equi},p}(y_0 + \Delta y) - U_{\mathrm{equi},n}(x_0 + \Delta x) = U_{\mathrm{equi},p}\left(y_0 + \frac{I\Delta t}{c_{s,p,\max} A \delta_p \varepsilon_{s,p} F}\right) - U_{\mathrm{equi},n}\left(x_0 - \frac{I\Delta t}{c_{s,n,\max} A \delta_n \varepsilon_{s,n} F}\right) \tag{11}$$

where $x$, $y$ are stoichiometric numbers, $U_{\mathrm{equi}}$ is equilibrium potential, $c_{s,\max}$ is maximum concentration in solid phase, $A$ is sandwich area and $F$ is Faraday constant. Subscripts $n$ and $p$ denote negative electrode (anode) and positive electrode (cathode), respectively. Since $\Delta y$ is positive and $\Delta x$ is negative, the discharged cell has a decreased $U_{\mathrm{equi},p}$, increased $U_{\mathrm{equi},n}$ and decreased OCV. However, for a degraded cell with smaller $\varepsilon_{s,n}$, the increase in $U_{\mathrm{equi},n}$ becomes larger in the same discharge process, which causes OCV to decrease faster under discharge. Therefore, the decrease in $\varepsilon_{s,n}$ leads to capacity fade. A detailed derivation and analysis of Eq. (11) are provided in Appendix A to study the effect of $\varepsilon_{s,n}$ on capacity fade.

The estimated total resistance obtained from SEI and deposit layer, $R_{\mathrm{SEI+DL}}$, are plotted in Fig. 21, where the resistance increases as the number of cycles increases. At 25 °C, the resistance increases mostly in the first 200 cycles but at 40 °C and 0 °C in the first 100 cycles. When the number of cycles becomes larger, the resistance increases as the temperature increases. The increase of the resistance indicates that deposits accumulate at the surface of anode and decrease ionic conductance of SEI.

The dimensionless diffusion coefficient of the electrolyte, $D_e^*$, is defined as $D_e$ of the degraded cell over $D_e$ of the fresh cell. $D_e^*$ is plotted in Fig. 22 as a function of the number of cycles and different ambient temperatures. $D_e^*$ decreases as the number of cycles

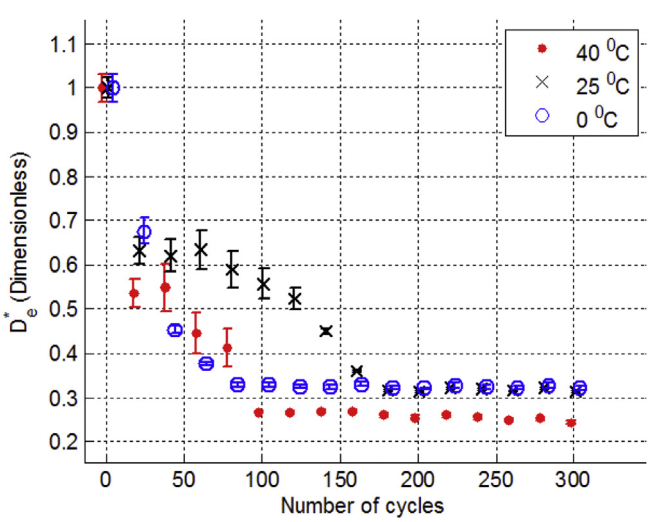


**Fig. 22.** Diffusion coefficient of electrolyte vs. number of cycles at different temperatures.

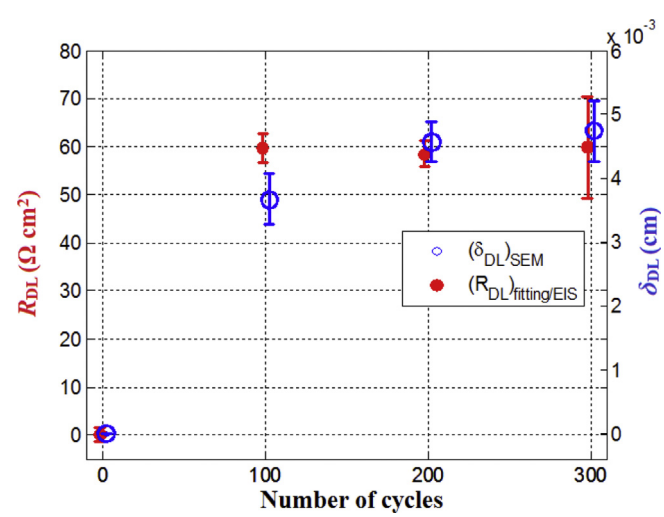


**Fig. 24.** $R_{DL}$ vs. $(\delta_{DL})_{SEM}$ for cells cycled at 40 °C.

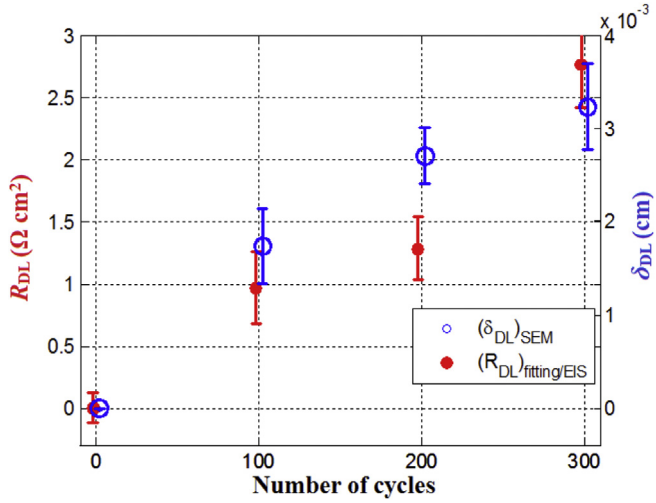


**Fig. 25.** $R_{DL}$ vs. $(\delta_{DL})_{SEM}$ for cells cycled at 0 °C.

increases and the effects of temperature on the coefficient are similar to the other parameters. The decrease of $D_e^*$ is predominantly caused by consumption of solvent of electrolyte.

The analysis of the effects of the parameters on degradation has shown that the degradation speeds up at the beginning of cycling and slows down after a certain number of cycles. The severe degradation at the beginning might be interpreted by the phenomena that the deposits isolate the anode particles that can be easily isolated because of relative small particle size and poor contact with composite anode. Once these particles have been isolated, isolation of the rest particles is difficult and consequently the capacity fade slows down.

The degradation processes by side reactions are also affected by ambient temperatures. The higher the temperature is, the more has degradation induced. Cycling cells at 40 °C and 25 °C has high degradation that at 0 °C. During the first 150 cycles, however, the degradation at 0 °C is severer than that at 25 °C because of increased SEI resistance in low temperature. The increase of the SEI resistance leads to a high rate of heat generation that can produce a high temperature locally at the interface between anode particles and electrolyte and accelerate the side reaction, even at the ambient temperature of 0 °C. As a result, the degradation process is fast. After 150 cycles, the capacity has largely decreased and the associated charging duration as well as heat generation in SEI has decreased, so the degradation process becomes slow. In addition, other degradation mechanisms might be involved like lithium plating [9] that forms at low temperature.

### 5.3. Validation of the resistance of deposit layer using SEM

One of the extracted parameters for degradation model is the resistance that consists of two parts, one from SEI and another from deposit layer, as shown in Fig. 21. The resistance of SEI, $(R_{SEI})_{EIS}$, was measured using EIS, as shown in Fig. 8. Therefore, the resistance of the deposit layer can be calculated by the difference between the estimated total resistance of SEI and deposit, and the resistance of SEI measured by EIS

$$R_{DL} = R_{SEI+DL} - (R_{SEI})_{EIS} \tag{12}$$

On the other hand, the thickness of the formed deposit layer, $(\delta_{DL})_{SEM}$, at different temperatures was measured by SEM, as shown in Fig. 11. Comparisons between the measured thickness of the deposit layer and the resistance of the $R_{DL}$ at different temperatures are shown in Figs. 23, 24 and 25, where the error bars of $(\delta_{DL})_{SEM}$ are the standard deviation of the measurements obtained from different samples of a cell.

At a given temperature, both $R_{DL}$ and $(\delta_{DL})_{SEM}$ increase as the number of cycles increases and are in good agreement. However, the value of $R_{DL}$ is significantly different at different temperatures, which implies dependence of the conductivity of the deposit layer on temperature.

This conductivity dependence is estimated by

$$\sigma_{DL} = \frac{\Delta(\delta)_{SEM}}{\Delta R_{DL}} \tag{13}$$

where $\Delta R_{DL}$ and $\Delta(\delta)_{SEM}$ are based on the results in Figs. 23, 24 and 25.

The conductivity of the deposit layer, $\sigma_{DL}$, at 0, 25 and 40 °C was 1.37, 0.16 and 0.08 S cm$^{-1}$, respectively. $\sigma_{DL}$ at 25 °C is twice as large as $\sigma_{DL}$ at 40 °C. The large variation might result from different compositions and structures of the deposits. In addition, $\sigma_{DL}$ at 0 °C is much higher than $\sigma_{DL}$ at the two other temperatures, which might be caused by the mixture of formed deposits and lithium plating [9] at low temperature. Thus, the conductivity of the deposit layer appears much higher.

## 6. Conclusions

Experimental investigations on material degradation of a pouch type NMC/Carbon battery using SEM, XRD and XPS have revealed that the major degradation is caused by deposits from side reactions at the anode. Based on these results and an electrochemical thermal model, three key parameters are identified and extracted from the terminal voltages obtained during cycles. These parameters are the volume fraction of accessible anode ($\varepsilon_{s,n}$), resistance of SEI and deposit layer ($R_{SEI+DL}$), and diffusion coefficient of electrolyte ($D_e$). The set of parameters are incorporated into the electrochemical model, whose performance is compared with the experimental data. In addition, effects of those parameters on degradation processes are analyzed. Particularly, the validity of the estimated resistance of the deposit layer is shown by measurement of its thickness using SEM. Key findings are summarized as follows:

- The anode particles are coated by deposits composed of $Li_2CO_3$, which is known as the product of the side reactions that is conductive to ions but nonconductive to electrons, but no phase change of active materials has been observed.
- The deposits lead to growth of SEI layer and increase in ionic resistance causing power fade. In addition, they electronically isolate certain anode particles, reducing the amount of active material and causing capacity fade. This hypothesis is manifested by the simulation results of the decrease in volume fraction of accessible active anode and increase in SEI resistance that are predicted using the model.
- The deposits of the side reactions also formed thick deposit layers coated between composite anode and separator. The deposit layer has lower ion conductivity than that of electrolyte and causes extra power fade. The resistance of the deposit layer estimated by the model has the same trend as its thickness measured by SEM.
- The dryness of the separator was observed which is most likely caused by the consumption of solvent of electrolyte. This process can decrease the diffusion coefficient of electrolyte, which are predicted using the model.
- At elevated temperature (40 °C), the side reactions are more extensive and more deposits are formed, according to the

experimental results and model predictions. The conductivity of deposits is smaller if the cell is cycled at higher temperature.

Future work will include developing physical equations that describe the side reactions and effect of current amplitude on degradation process.

**Acknowledgment**

This project is funded by General Motors Corporation, USA. The authors do appreciate the financial support and technical discussions.

## Appendix A. Analysis of effect $\varepsilon_{s,n}$ on capacity fade

The derivation of Eq. (11) is shown in following procedure. Assume a cell has an initial OCV that is

$$\mathrm{OCV}_0 = U_{\mathrm{equi},p}(y_0) - U_{\mathrm{equi},n}(x_0) \tag{A.1}$$

When it is discharged by a constant current $I$ for a duration of $\Delta t$, the amount of Li ion that moved from anode to cathode would be

$$\Delta n = \frac{I\Delta t}{F} \tag{A.2}$$

where $F$ is Faraday constant. The change in average concentration at anode side is

$$\Delta\bar{c}_{s,n} = -\frac{\Delta n}{V_n\varepsilon_{s,n}} = -\frac{I\Delta t}{A\delta_n\varepsilon_{s,n}F} \tag{A.3}$$

where $V_n$ is the volume of composite anode. The change in $\bar{c}_{s,n}$ would cause change in the stoichiometric number and equilibrium potential of anode

$$\begin{aligned} U_{\mathrm{equi},n}(x_0+\Delta x) &= U_{\mathrm{equi},n}\left(x_0 + \frac{\overline{\Delta c}_{s,n}}{c_{s,n,\max}}\right) \\ &= U_{\mathrm{equi},n}\left(x_0 - \frac{I\Delta t}{c_{s,n,\max}A\delta_n\varepsilon_{s,n}F}\right) \end{aligned} \tag{A.4}$$

where $x$ is the stoichiometric number of anode. In the discharge process, $x$ decreases and $U_{\mathrm{equi},n}$ increases. At the same time, the cathode side acquired $\Delta n$ mol Li ion from the anode. Similarly, the equilibrium potential of cathode would be changed to

$$\begin{aligned} U_{\mathrm{equi},p}(y_0+\Delta y) &= U_{\mathrm{equi},p}\left(y_0 + \frac{\overline{\Delta c}_{s,p}}{c_{s,p,\max}}\right) \\ &= U_{\mathrm{equi},p}\left(y_0 + \frac{I\Delta t}{c_{s,p,\max}A\delta_p\varepsilon_{s,p}F}\right) \end{aligned} \tag{A.5}$$

where $y$ is the stoichiometric number of cathode. In contrast, $y$ increases and $U_{\mathrm{equi},p}$ decreases in the discharge process. Therefore, the OCV after discharge can be calculated as the difference between $U_{\mathrm{equi},p}$ and $U_{\mathrm{equi},n}$

$$\begin{aligned} \mathrm{OCV} &= U_{\mathrm{equi},p}(y_0+\Delta y) - U_{\mathrm{equi},n}(x_0+\Delta x) \\ &= U_{\mathrm{equi},p}\left(y_0 + \frac{I\Delta t}{c_{s,p,\max}A\delta_p\varepsilon_{s,p}F}\right) \\ &\quad - U_{\mathrm{equi},n}\left(x_0 - \frac{I\Delta t}{c_{s,n,\max}A\delta_n\varepsilon_{s,n}F}\right) \end{aligned} \tag{A.6}$$

To study the effect of volume fraction of anode, $\varepsilon_{s,n}$, on cell capacity, $Q_{\max}$, the equation above is used to analyze a complete discharge process ranged from100% SOC ($x_0 = x_{\max}$) to 0% SOC ($x_0 + \Delta x = x_{\min}$), where

$$\Delta x = x_{\min} - x_{\max} = -\frac{I\Delta t}{c_{s,n,\max}A\delta_n\varepsilon_{s,n}F} \tag{A.7}$$

Then, the capacity can be expressed as follows

$$Q_{\max} = \int_{100\%}^{0\%} I dt = I\Delta t = c_{s,n,\max}A\delta_n\varepsilon_{s,n}F(x_{\max} - x_{\min}) \tag{A.8}$$

The equation shows that cell capacity tends to follow changes of $\varepsilon_{s,n}$. Since no changes in volume fraction of cathode, $\varepsilon_{s,p}$, is assumed, the decrease in $\varepsilon_{s,n}$ causes capacity imbalance between anode and cathode. As a result the capacity of a degraded cell is limited by the capacity of anode.

## Appendix B. Modeling parameters (fresh cell)

| Category | Parameter | Negative electrode | Separator | Positive electrode | Unit |
|---|---|---|---|---|---|
| Geometry and volume fractions | Thickness, $\delta$ | $50 \times 10^{-4}$ | $25.4 \times 10^{-4}$ | $36.4 \times 10^{-4}$ | cm |
| | Particle radius, $r_s$ | $1 \times 10^{-4}$ | | $1 \times 10^{-4}$ | cm |
| | Active material volume fraction, $\varepsilon_s$ | 0.58 | | 0.5 | |
| | Polymer phase volume fraction, $\varepsilon_p$ | 0.048 | 0.5 | 0.11 | |
| | Conductive filler volume fraction, $\varepsilon_f$ | 0.04 | | 0.06 | |
| | Porosity, $\varepsilon_e$ | 0.332 | 0.5 | 0.33 | |
| $Li^+$ concentrations | Stoichiometry at 0% SOC: $x_{0\%}$, $y_{0\%}$ | 0.126 | | 0.936 | |
| | Stoichiometry at 100% SOC: $x_{100\%}$, $y_{100\%}$ | 0.676 | | 0.442 | |
| | Average electrolyte concentration, $c_e$ | $1.2 \times 10^{-3}$ | $1.2 \times 10^{-3}$ | $1.2 \times 10^{-3}$ | mol cm$^{-3}$ |
| | Exchange current density coefficient, $k_{i0}$ | 12.9 | | 6.28 | A cm$^{-2}$ |
| Kinetic and transport properties | Charge-transfer coefficient, $\alpha_a$, $\alpha_c$ | 0.5, 0.5 | | 0.5, 0.5 | |
| | Solid phase diffusion coefficient, $D$ | $2.0 \times 10^{-12}$ | | $3.7 \times 10^{-12}$ | cm$^2$ s$^{-1}$ |
| | Solid phase conductivity, $\sigma$ | 1 | | 0.1 | S cm$^{-1}$ |
| | Electrolyte phase $Li^+$ diffusion coefficient, $D_e$ | $2.6 \times 10^{-6}$ | $2.6 \times 10^{-6}$ | $2.6 \times 10^{-6}$ | cm$^2$ s$^{-1}$ |
| | Bruggeman's porosity exponent, $p$ | 1.5 | 1.5 | 1.5 | |
| | Electrolyte phase ionic conductivity, $\kappa$ | $15.8\ c_e \exp(-13{,}472\ c_e^{1.4})$ | | $15.8\ c_e \exp(-13472\ c_e^{1.4})$ | S cm$^{-1}$ |
| | $Li^+$ transference number, $t_+^0$ | 0.363 | 0.363 | 0.363 | |

## References


[1] P. Ramadass, B. Haran, P. Gomadam, R. White, B. Popov, J. Electrochem. Soc. 151 (2004) A196–A203.
[2] P. Arora, R. White, M. Doyle, J. Electrochem. Soc. 145 (1998) 3647–3667.
[3] S. Santhanagopalan, Q. Zhang, K. Kumaresan, R. White, J. Electrochem. Soc. 155 (2008) A345–A353.
[4] G. Sikha, B. Popov, R. White, J. Electrochem. Soc. 151 (2004) A1104–A1114.
[5] H. Ploehn, P. Ramadass, R. White, J. Electrochem. Soc. 151 (2004) A456–A462.
[6] Q. Zhang, R. White, J. Power Sources 179 (2008) 793–798.
[7] D. Aurbach, M. Levi, E. Levi, A. Schechter, J. Phys. Chem. B 101 (1997) 2195–2206.
[8] P. Verma, P. Maire, P. Novak, Electrochim. Acta 55 (2010) 6332–6341.
[9] J. Vetter, P. Novak, M. Wagner, C. Veit, K. Moller, J. Besenhard, M. Winter, M. Wohlfahrt-Mehrens, C. Vogler, A. Hammouche, J. Power Sources 147 (2005) 269–281.
[10] S. Shi, P. Lu, Z. Liu, Y. Qi, L. Hector, H. Li, S. Harris, J. Am. Chem. Soc. 134 (2012) 15476–15487.
[11] P. Ramadass, B. Haran, R. White, B. Popov, J. Power Sources 111 (2002) 210–220.
[12] K. Schroder, H. Celio, L. Webb, K. Stevenson, J. Phys. Chem. C 116 (2012) 19737–19747.
[13] D. Abraham, R. Twesten, M. Balasubramanian, I. Petrov, J. McBreen, K. Amine, Electrochem. Commun. 4 (2002) 620–625.
[14] I. Isaev, G. Salitra, A. Soffer, Y. Cohen, D. Aurbach, J. Fischer, J. Power Sources 119–121 (2003) 28–33.
[15] H. Wang, Y. Jang, B. Huang, D. Sadoway, Y. Chiang, J. Electrochem. Soc. 146 (1999) 473–480.
[16] J. Li, E. Murphy, J. Winnick, P. Kohl, J. Power Sources 102 (2001) 294–301.
[17] R. Kostecki, F. McLarnon, J. Power Sources 119 (2003) 550–554.
[18] D. Zhang, B. Haran, A. Durairajan, R. White, Y. Podrazhansky, B. Popov, J. Power Sources 91 (2000) 122–129.
[19] D. Jang, Y. Shin, S. Oh, J. Electrochem. Soc. 143 (1996) 2204–2211.
[20] S. Santhanagopalan, Q. Guo, P. Ramadass, R. White, J. Power Sources 156 (2006) 620–628.
[21] P. Ramadass, B. Haran, R. White, B. Popov, J. Power Sources 123 (2003) 230–240.
[22] S. Choi, H. Lim, J. Power Sources 111 (2002) 130–136.
[23] R. Fu, M. Xiao, S.Y. Choe, J. Power Sources 224 (2012) 211–224.
[24] J. Morales, R. Trocoli, S. Franger, J. Santos-Pena, Electrochim. Acta 55 (2010) 3075–3082.
[25] Y. Shao-Horn, S. Hackney, C. Johnson, A. Kahaian, M. Thackeray, J. Solid State Electrochem. 140 (1998) 116.
[26] K. Aifantis, J. Dempsey, J. Power Sources 143 (2005) 203–211.
[27] A. Millner, in: IEEE Conference on Innovative Technologies for an Efficient and Reliable Electricity Supply, 2010.
[28] Y. Gao, J. Dahn, Solid State Ionics 84 (1996) 33–40.
[29] K. Aifantis, S. Hackney, J. Dempsey, J. Power Sources 165 (2007) 874–879.
[30] R. Bouchet, S. Lascaud, M. Rosso, J. Electrochem. Soc. 150 (2003) A1385–A1389.
[31] P. Moss, G. Au, E. Plichta, J. Zheng, J. Electrochem. Soc. 157 (2010) A1–A7.
[32] G. Ning, B. Haran, B. Popov, J. Power Sources 117 (2003) 160–169.
[33] B. Ratnakumar, M. Smart, S. Surampudi, in: Battery Conference on Applications and Advances, The Seventeenth Annual, 2002.
[34] S. Contarni, J.W. Rabalais, J. Electron Spectrosc. Relat. Phenom. 35 (1985) 191.
[35] J.P. Contour, A. Salesse, M. Froment, M. Garreau, J. Thevenin, D. Warin, J. Microsc. Spectrosc. Electron. 4 (1979) 483.
[36] M. Xiao, S. Choe, J. Power Sources 218 (2012) 357–367.